Draft version September 19, 2025
Typeset using LaTeX **twocolumn** style in AASTeX62

# DELVE-DEEP Survey: The Faint Satellite System of NGC 55

Jonah Medoff,[1,2] Burçın Mutlu-Pakdil,[3] Jeffrey L. Carlin,[4] Alex Drlica-Wagner,[1,5,6] Erik J. Tollerud,[7] Amandine Doliva-Dolinsky,[8,3] David J. Sand,[9] Clara E. Martínez-Vázquez,[10] Guy S. Stringfellow,[11] William Cerny,[12] Denija Crnojević,[8] Peter S. Ferguson,[13] Catherine E. Fielder,[9] Astha Chaturvedi,[14] Nitya Kallivayalil,[15] Noelia E. D. Noël,[14] Kathy Vivas,[16] Alistair R. Walker,[16] Monika Adamów,[17] Clecio R. Bom,[18] Julio A. Carballo-Bello,[19] Yumi Choi,[20] Gustavo E. Medina,[21] Mahdieh Navabi,[14] Andrew B. Pace,[15] Alex H. Riley,[22] and Joanna D. Sakowska[14,23]
(DELVE Collaboration)

[1] *Department of Astronomy and Astrophysics, University of Chicago, Chicago, IL 60637, USA*
[2] *Department of Physics, Harvard University, 17 Oxford St, Cambridge, MA 02138, USA*
[3] *Department of Physics and Astronomy, Dartmouth College, Hanover, NH 03755, USA*
[4] *Rubin Observatory/AURA, 950 North Cherry Avenue, Tucson, AZ, 85719, USA*
[5] *Fermi National Accelerator Laboratory, P. O. Box 500, Batavia, IL 60510, USA*
[6] *Kavli Institute for Cosmological Physics, University of Chicago, Chicago, IL 60637, USA*
[7] *Space Telescope Science Institute, 3700 San Martin Drive, Baltimore, MD 21218, USA*
[8] *Department of Physics and Astronomy, University of Tampa, 401 West Kennedy Boulevard, Tampa, FL 33606, USA*
[9] *Steward Observatory, University of Arizona, 933 North Cherry Avenue, Tucson, AZ 85721-0065, USA*
[10] *International Gemini Observatory/NSF NOIRLab, 670 N. A'ohoku Place, Hilo, Hawai'i, 96720, USA*
[11] *Center for Astrophysics and Space Astronomy, University of Colorado, 389 UCB, Boulder, CO 80309-0389, USA*
[12] *Department of Astronomy, Yale University, New Haven, CT 06520, USA*
[13] *DIRAC Institute, Department of Astronomy, University of Washington, 3910 15th Ave NE, Seattle, WA, 98195, USA*
[14] *Department of Physics, University of Surrey, Guildford GU2 7XH, UK*
[15] *Department of Astronomy, University of Virginia, 530 McCormick Road, Charlottesville, VA 22904, USA*
[16] *Cerro Tololo Inter-American Observatory/NSF NOIRLab, Casilla 603, La Serena, Chile*
[17] *Center for Astrophysical Surveys, National Center for Supercomputing Applications, 1205 West Clark St., Urbana, IL 61801, USA*
[18] *Centro Brasileiro de Pesquisas Físicas, Rua Dr. Xavier Sigaud 150, 22290-180 Rio de Janeiro, RJ, Brazil*
[19] *Instituto de Alta Investigación, Universidad de Tarapacá, Casilla 7D, Arica, Chile*
[20] *NSF NOIRLab, 950 N. Cherry Ave., Tucson, AZ 85719, USA*
[21] *Department of Astronomy and Astrophysics, University of Toronto, 50 St. George Street, Toronto ON, M5S 3H4, Canada*
[22] *Institute for Computational Cosmology, Department of Physics, Durham University, South Road, Durham DH1 3LE, UK*
[23] *Instituto de Astrofísica de Andalucía, CSIC, Glorieta de la Astronomía, E-18080 Granada, Spain*

## ABSTRACT

We report the first comprehensive census of the satellite dwarf galaxies around NGC 55 (2.1 Mpc) as a part of the DECam Local Volume Exploration DEEP (DELVE-DEEP) survey. NGC 55 is one of four isolated, Magellanic analogs in the Local Volume around which DELVE-DEEP aims to identify faint dwarfs and other substructures. We employ two complementary detection methods: one targets fully resolved dwarf galaxies by identifying them as stellar overdensities, while the other focuses on semiresolved dwarf galaxies, detecting them through shredded unresolved light components. As shown through extensive tests with injected galaxies, our search is sensitive to candidates down to $M_V \lesssim -6.6$ and surface brightness $\mu \lesssim 28.5$ mag arcsec$^2$, and $\sim 80\%$ complete down to $M_V \lesssim -7.8$. We do not report any new confirmed satellites beyond two previously known systems, ESO 294-010 and NGC 55-dw1. We construct the satellite luminosity function of NGC 55 and find it to be consistent with the predictions from cosmological simulations. As one of the first complete luminosity functions for a Magellanic analog, our results provide a glimpse of the constraints on low-mass-host satellite

Corresponding author: Jonah Medoff
jmedoff@fas.harvard.edu

populations that will be further explored by upcoming surveys, such as the Vera C. Rubin Observatory's Legacy Survey of Space and Time.

## 1. INTRODUCTION

The ΛCold Dark Matter (ΛCDM) cosmological model has been well assessed on large scales, with observations of the large-scale structure of the Universe and cosmic microwave background providing strong support for its predictions (e.g., DES Collaboration et al. 2018; Planck Collaboration et al. 2020). In comparison, observational constraints on the small-scale distribution of dark matter are relatively limited (Bullock & Boylan-Kolchin 2017). Dwarf galaxies, being the most ancient, metal-poor, and dark-matter-dominated galaxies in the Universe, serve as excellent probes of early galaxy formation and small-scale dark matter distribution (Simon 2019), thus providing a means of exploring ΛCDM on small scales (Bullock & Boylan-Kolchin 2017). Within the last 20 years, dozens of dwarf galaxies have been discovered around the Milky Way (MW; e.g, Willman et al. 2005; Belokurov et al. 2006; Simon & Geha 2007; Bechtol et al. 2015; Drlica-Wagner et al. 2015; Koposov et al. 2015; Mau et al. 2020; Cerny et al. 2021a,b, 2023; Homma et al. 2024) and other MW-mass hosts (e.g., M31: Martin et al. 2013, Doliva-Dolinsky et al. 2022, 2023, Arias et al. 2025, Smith et al. 2025; M81: Chiboucas et al. 2009; Cen A: Crnojević et al. 2016, 2019; M94: Smercina et al. 2018; M101: Bennet et al. 2019, 2020; NGC 253: Mutlu-Pakdil et al. 2024; ELVES: Carlsten et al. 2022; SAGA: Mao et al. 2024).

In order to thoroughly assess the small-scale predictions of ΛCDM, we need to explore satellite systems in host environments with lower masses than the MW to better understand how astrophysical processes, such as the effects of reionization, tidal and ram pressure stripping, and host infall time, affect satellite populations (Drlica-Wagner et al. 2021). Ideally, we could study these effects using the Magellanic Clouds (MCs), but, due to their location within the MW halo, the association of some satellites between the MCs and MW remains ambiguous (e.g., Jethwa et al. 2016; Patel et al. 2020; Cerny et al. 2021a). Furthermore, satellites that are known to be bound to the MCs have likely experienced recent interactions with the MW, complicating the interpretation of their gas contents, stellar populations, and orbital dynamics. As a result, we must search for satellites of isolated, MC-mass hosts beyond the Local Group. Several studies in recent years have already begun to perform such searches (e.g., Sand et al. 2015, 2024; MADCASH: Carlin et al. 2016, 2021, 2024; LBT-SONG: Davis et al. 2021; ELVES-Dwarf: Li et al. 2025; ID-MAGE: Hunter et al. 2025), discovering several dwarf satellites around MC analogs in the Local Volume, such as NGC 3109, NGC 4124, and NGC 628, and the first complete satellite census of an MC-mass host (NGC 2403) was recently presented in Carlin et al. (2024). To sufficiently test ΛCDM on small scales, however, it is necessary to study the satellite populations of a larger sample of MC-mass hosts.

As part of the DEEP component of the DECam Local Volume Exploration (DELVE-DEEP; Drlica-Wagner et al. 2021, 2022) survey, we perform a comprehensive dwarf satellite search around NGC 55, a barred spiral galaxy located at ∼2.1 Mpc, with a mass and morphology similar to the LMC (de Vaucouleurs et al. 1991; Dalcanton et al. 2009; Westmeier et al. 2013). NGC 55 is considered to be a member of the Sculptor Group, but given the weak gravitational bound of the Group (Jerjen et al. 1998; Karachentsev et al. 2003) and the low tidal index[1] of NGC 55 ($\Theta_5 = 0.1$; Karachentsev et al. 2013), it is likely to only be loosely bound to this group. Within its local environment, NGC 55 has several nearby neighbors: NGC 300 ($D_{\rm proj} \sim 278.2$ kpc) and two dwarf spheroidal (dSph) galaxies, ESO 410-005 ($D_{\rm proj} \sim 244.8$ kpc) and ESO 294-010 ($D_{\rm proj} \sim 120.8$ kpc). The latter of these dSphs is located at the edge of the virial radius of NGC 55 (see Table 1) and is a likely satellite companion, judging by its tip of the red-giant-branch (TRGB) distance and radial velocity ($D = 2.0$ Mpc; $v_r = 117$ km/s; McConnachie 2012).

Using the high-resolution, dark-matter-only *Caterpillar* suite of simulations (Griffen et al. 2016) and stellar mass-halo mass relation of Garrison-Kimmel et al. (2016), Dooley et al. (2017) predicts that an LMC-mass host like NGC 55 should host a total of 2-6 satellite galaxies with $M_V \leq -7$. In addition to ESO 294-010 ($M_V \sim -11.3$; Karachentsev et al. 2002), a second, more diffuse dwarf satellite of NGC 55, NGC 55-dw1 ($M_V \sim -8.0$), was recently identified using Dark Energy Survey (DES) Year 6 and DELVE-DEEP data and presented in McNanna et al. (2024). Taking these known dwarfs into account, the predictions of Dooley et al. (2017) suggest that there should be 0-4 remaining dwarfs detectable within our data. The basic properties of NGC 55 and its two known satellites are listed in Table 1.

Previous satellite searches around isolated, low-mass hosts have utilized either resolved star detection methods (e.g., Carlin et al. 2016, 2021) or integrated light

[1] The tidal index, $\Theta_5$, is a measure of the cumulative gravitational influence of a galaxy's five most significant neighbors (see Karachentsev et al. 2013 for definition).

**Table 1.** Properties of NGC 55, ESO 294-010, and NGC 55-dw1

| Parameter | NGC 55 | ESO 294-010 | NGC 55-dw1 | References |
|---|---|---|---|---|
| R.A. (deg) | $00^h14^m53^s.6$ | $00^h26^m33^s.5$ | $00^h15^m28^s.8$ | NED (1) |
| Decl. (deg) | -39°11'47".9 | -41°51'18".2 | -38°25'08".4 | NED (1) |
| Distance (Mpc) | 2.1 | 2.0 | 2.2 | (2, 3, 1) |
| Radial Velocity (km/s) | 129 | 117 | ... | (3) |
| Stellar Mass ($M_\odot$) | $3.0 \times 10^9$ | $2.7 \times 10^6$ | ... | (4, 3) |
| Virial Radius (kpc) | 120 | ... | ... | (5) |
| $M_V$ (mag) | -18.6 | -11.3 | -8.0 | (6, 7, 1) |
| $r_h$ (pc) | 3916 | 248 | 2200 | (8, 3, 1) |
| $r_h$ (arcsec) | 385 | 24 | 220 | (8, 3, 1) |
| $\mu_{\rm eff}$ (mag arcsec$^{-2}$) | 22.8 | 24.1 | 32.3 | (8, 7, 3, 1) |
| $D_{\rm proj}$ (kpc) | N/A | 120.8 | 30.2 | NED (1) |

**References:** (1) McNanna et al. 2024, (2) Dalcanton et al. 2009, (3) McConnachie 2012, (4) Dooley et al. 2017, (5) Mutlu-Pakdil et al. 2021, (6) Gil de Paz et al. 2007, (7) Karachentsev et al. 2002, (8) Moustakas et al. 2023

detection methods (e.g., Davis et al. 2021). While these two methods have been effective, neither method, on their own, spans the entire size-luminosity parameter space of known dwarf galaxies. To address this, we implement a new approach that combines both a resolved and "semiresolved" search for dwarf galaxies (see Section 3.2 for a definition of semiresolved). Through extensive tests with injected galaxies (see Section 4), we show that this method is sensitive to a parameter space of dwarfs that extends well beyond those of previous satellite searches (at the distance of NGC 55).

In this work, we present the results of our systematic NGC 55 satellite search, along with our resulting satellite luminosity function (LF) for NGC 55 down to a limit of $M_V \sim -7$. Section 2 presents an overview of the DELVE-DEEP survey. Section 3 outlines our approach for detecting dwarf galaxy satellites and the results obtained. Section 4 details our methodology for performing artificial dwarf galaxy simulations, along with our assessment of the detection sensitivity and completeness. In Section 5, we present the satellite LF of NGC 55 and place its satellite system in context with other known systems, and, finally, in Section 6, we summarize our conclusions.

## 2. THE DELVE-DEEP SURVEY AND DATA PROCESSING

DELVE is a multicomponent survey using the Dark Energy Camera (Flaugher et al. 2015) on the Blanco 4m Telescope at the Cerro Tololo Inter-American Observatory that aims to characterize satellite galaxy populations across a range of environments in the Local Volume (Drlica-Wagner et al. 2021). DELVE-DEEP is one of the three components of this survey that specifically targets isolated MC analogs beyond the Local Group to study their dwarf satellite populations and other substructures within their halo. DELVE-DEEP obtained 135 deg$^2$ of deep imaging in the $g$ and $i$ optical bands around four MC-mass host galaxies at 1.4-2.1 Mpc: two LMC-mass analogs (NGC 55 and NGC 300) and two SMC-mass analogs (Sextans B and IC 5152). This program is complementary to the MADCASH survey (Carlin et al. 2016, 2021, 2024), which aims to investigate the satellite populations and substructures of seven additional MC-mass hosts in the Local Volume (two of which have been completed; see Carlin et al. 2024 and Doliva-Dolinsky et al. 2025). Recently, several stellar substructures were discovered around NGC 300 using DELVE-DEEP data and are presented in Fielder et al. (2025). NGC 55, however, is the first of the four DELVE-DEEP targets around which we have performed a comprehensive dwarf galaxy satellite search.

The DELVE-DEEP observations of NGC 55 were collected on 17 distinct nights between 2019 August and 2021 July and performed over 14 distinct fields within a 3.25 deg radius from the galactic center, which roughly corresponds to the virial radius of NGC 55 ($r_{\rm vir} \sim$ 120 kpc). Within each field, 12 $g$-band exposures and 7 $i$-band exposures were taken, each with an exposure time of 300 s and good seeing (FWHM $<$ 1.0 arcsec). Combined with the DES exposures in these fields, this gives a total of 15×300 s exposures in $g$ and 10×300 s exposures in $i$ (Drlica-Wagner et al. 2021). Across all fields, the median point-spread function (PSF) FWHM was 0.97″ in $g$ and 0.82″ in $i$. Additionally, each observation within each field was dithered by 4′ in R.A. and 2′ in decl. to mitigate chip gaps in the images and improve the uniformity of depth.

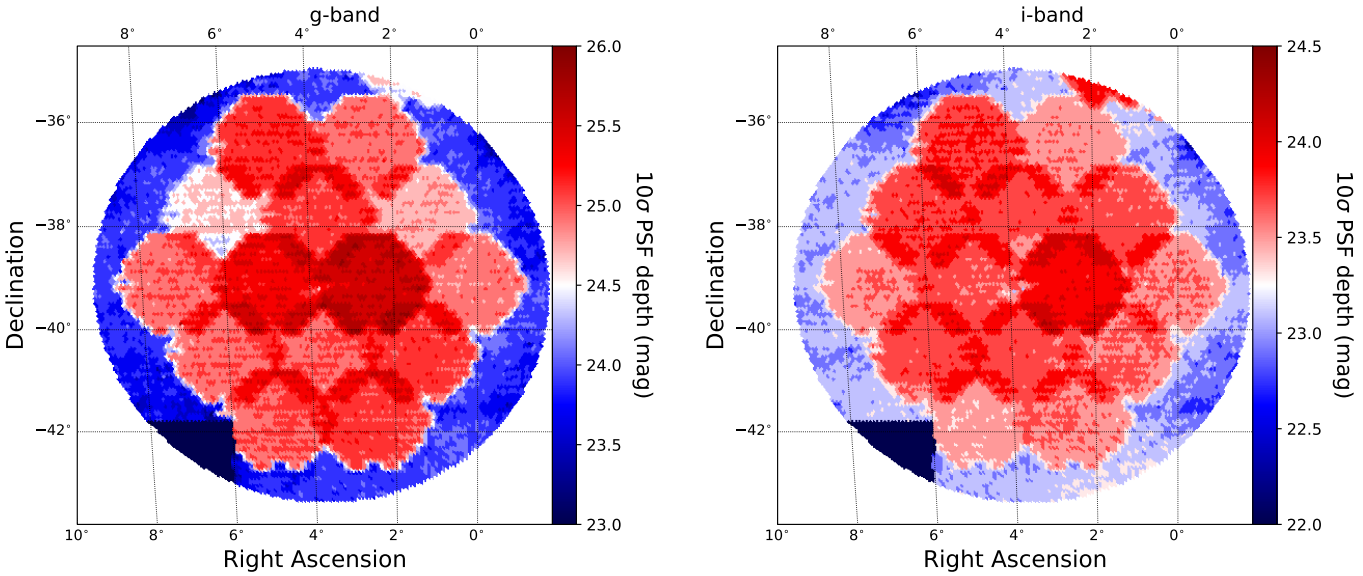


**Figure 1.** $10\sigma$ PSF depth of DECam photometry around NGC 55 in $g$ and $i$ optical bands. $10\sigma$ PSF depth is defined as the PSF magnitude at which the signal-to-noise ratio is equal to 10. The central red regions correspond to fields with both DELVE-DEEP and DES imaging, while the outer blue regions correspond to fields with only DES imaging. The field in the bottom left corner was imaged as part of the DES supernova program and was excluded from our dataset. The total region shown spans a projected physical radius of ∼150 kpc.

Image processing was performed via the DES Data Management pipeline (DESDM; Morganson et al. 2018; for a description of how the DESDM pipeline is applied to DELVE data, see Tan et al. 2024), which is based on `SourceExtractor` (Bertin & Arnouts 1996). Images of the sky are broken up into 0.73 deg$^2$ regions called "tiles" (Morganson et al. 2018). Despite DELVE-DEEP only using the $g$ and $i$ bands, our data processing requires both the detection image (which is a composite of $g$-, $r$-, and $i$-band tiles) and the single-band image ($g$ or $i$) for each field. `SourceExtractor` uses the detection image to identify sources and then performs forced photometry using the single-band image, which enhances its overall detection sensitivity. The same procedure is implemented in our dwarf galaxy simulations (see Section 4) to ensure consistency in detecting both real and artificial sources.

In addition to DESDM processing, extinction corrections were applied to all $g$- and $i$-band magnitudes according to the procedure described in Drlica-Wagner et al. (2021, 2022). Contrary to previous dwarf galaxy searches (e.g., Carlin et al. 2016), star-galaxy separation was not applied to the data. Our artificial dwarf galaxy simulations (see Section 4) reveal that, at the distance of NGC 55, blending and crowding of stars in the central regions of dwarf galaxies, combined with underlying diffuse light, lead to uncertain photometry that makes star-galaxy separation unreliable. As a result, many of these stars are classified as galaxies, which would cause many dwarf galaxies to go undetected in our search if star-galaxy separation was applied. Thus, to optimize the completeness of our dwarf search, we find it more effective not to apply star-galaxy separation. While this choice increases the number of false detections in our dwarf galaxy search, we mitigate this by visually inspecting each candidate (see Section 3.3). Although other PSF-fitting photometry programs, such as DAOPHOT (Stetson 1987), could potentially provide more reliable star-galaxy separation, applying these methods to the entire survey would have been significantly more time-consuming.

DELVE-DEEP has achieved average $10\sigma$ depths of $g = 25.1$ mag and $i = 23.7$ mag around NGC 55 (where $10\sigma$ depth is defined as the PSF magnitude at which the signal-to-noise ratio is equal to 10; see Figure 1), which is $\sim 1$ mag deeper than the corresponding DES imaging in this region (McNanna et al. 2024). Additionally, using artificial star tests (discussed in more detail in Appendix A), we determine that our observations are 90% complete to depths of $g_{90\%} = 25.3$ mag and $i_{90\%} = 24.6$ mag, providing sensitivity to resolved stars roughly 1.5 mag fainter than the TRGB ($m_g^{\rm TRGB} = 24.3$; $m_i^{\rm TRGB} = 22.6$).

## 3. DWARF SATELLITE SEARCH

In our dwarf search around NGC 55, we take a new approach and implement a pipeline that combines two distinct dwarf galaxy detection methods: one that detects dwarf galaxies containing primarily resolved red-giant-

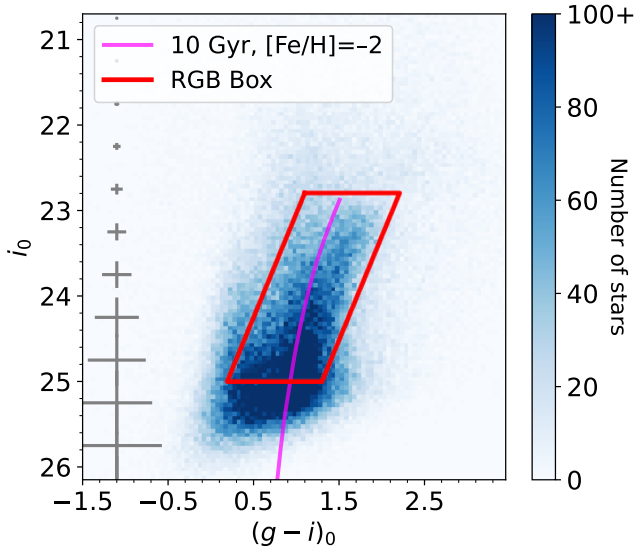


**Figure 2.** Binned color-magnitude diagram of the central region of NGC 55 with the RGB selection box used in our dwarf galaxy search displayed in red. This RGB box covers $i$-band magnitudes of $22.8 \leq i \leq 25.0$. An isochrone corresponding to stellar populations with age = 10 Gyr and metallicity [Fe/H] = −2 at the distance of NGC 55 is shown in magenta, which was generated using the Dartmouth Stellar Evolution Database (Dotter et al. 2008). Magnitude uncertainties (which come from the `SourceExtractor` parameter, `MAG_ERR`) are given in gray on the left.

branch (RGB) sources (Section 3.1), and one that detects dwarf galaxies containing a mix of resolved sources and shredded, unresolved light components (we refer to these dwarf galaxies as "semiresolved"; Section 3.2).

### 3.1. *Resolved Search*

Following previous dwarf galaxy searches (e.g., Martin et al. 2013; Crnojević et al. 2016; McQuinn et al. 2023, 2024; Carlin et al. 2024; McNanna et al. 2024; Mutlu-Pakdil et al. 2024), one way we identify dwarf galaxies is by using resolved RGB stars. This is because dwarf galaxies primarily consist of old, metal-poor stars, which have evolved off the main sequence onto the RGB. We identify potential RGB stars in our data based on the color-magnitude selection box shown in Figure 2. The boundaries of this selection box were chosen to cover all of the sources in our data along the RGB and are consistent with an isochrone of stellar populations with age = 10 Gyr and [Fe/H] = −2 (Dotter et al. 2008).

The sources within the RGB selection box are divided into 1.5 arcmin$^2$ spatial bins, and for each bin, mean and standard deviation background bin values (`MEAN_BKG_BIN` and `STD_BKG_BIN`) are calculated using the surrounding annulus of bins, with inner radius $2 * $ `binsize` and outer radius $3 * $ `binsize`. The resulting binned density map (see Figure 3) is run through a `photutils` function called `find_peaks` (Astropy Collaboration et al. 2013), with `threshold` = `MEAN_BKG_BIN` + $3 * $ `STD_BKG_BIN` (i.e., $3\sigma$ above the mean background value) and `box_size` = 3, which roughly corresponds to the expected size, in bin length, of a dwarf satellite of NGC 55. This function outputs 419 overdensities, or "peaks" (which include the previously discovered satellite, NGC 55-dw1), although many of these are false detections (e.g., overdensities of sources due to a background galaxy, a bright foreground star, or a background galaxy cluster), which are later filtered out through systematic visual inspection (see Section 3.3).

### 3.2. *Semiresolved Search*

In addition to fully resolved dwarf galaxies, we expect some dwarfs at the distance of NGC 55 to potentially contain a combination of resolved and unresolved stars. Consequently, such systems could go undetected by our resolved search method. These dwarf galaxies (which we refer to as "semiresolved" dwarfs) contain central regions of blended, unresolved light surrounded by more dispersed, resolved stars in the outskirts.

Through our artificial dwarf galaxy simulations (see Section 4), we find that `SourceExtractor` "shreds" the central, unresolved regions of these semiresolved dwarfs into several, distinct sources, each of which exhibits low surface brightness (LSB) and a large flux radius (for a definition and discussion of "shredding" in unresolved sources, see Prole et al. 2018). Since these sources cannot be detected by our resolved search, we implement a second detection method that targets overdensities of LSB sources. Note that this methodology differs from previous unresolved dwarf galaxy searches (e.g., Davis et al. 2021), which target single LSB sources, as opposed to shredded, LSB overdensities.

To select LSB sources, we utilize LSB selection criteria adapted from those listed in Tanoglidis et al. (2021). These criteria rely mostly on the `SourceExtractor` parameters, `FLUX_RADIUS` (defined as the radius of a circular isophote containing half of a source's flux) and `MU_EFF_MODEL` (effective surface brightness), and our corresponding selection cuts for these two parameters are:

```
(FLUX_RADIUS_G > 5) & (FLUX_RADIUS_G < 20),
(FLUX_RADIUS_I > 5) & (FLUX_RADIUS_I < 20),
(MU_EFF_MODEL_G > 24.2) & (MU_EFF_MODEL_G < 31.2).
```

We test several different selection cuts for these parameters, but find that these limits maximize the number of detected artificial dwarfs (see Section 4) without resulting in too many false detections in our real dwarf galaxy search. Our other LSB selection criteria come directly from Tanoglidis et al. (2021), but, in compari-

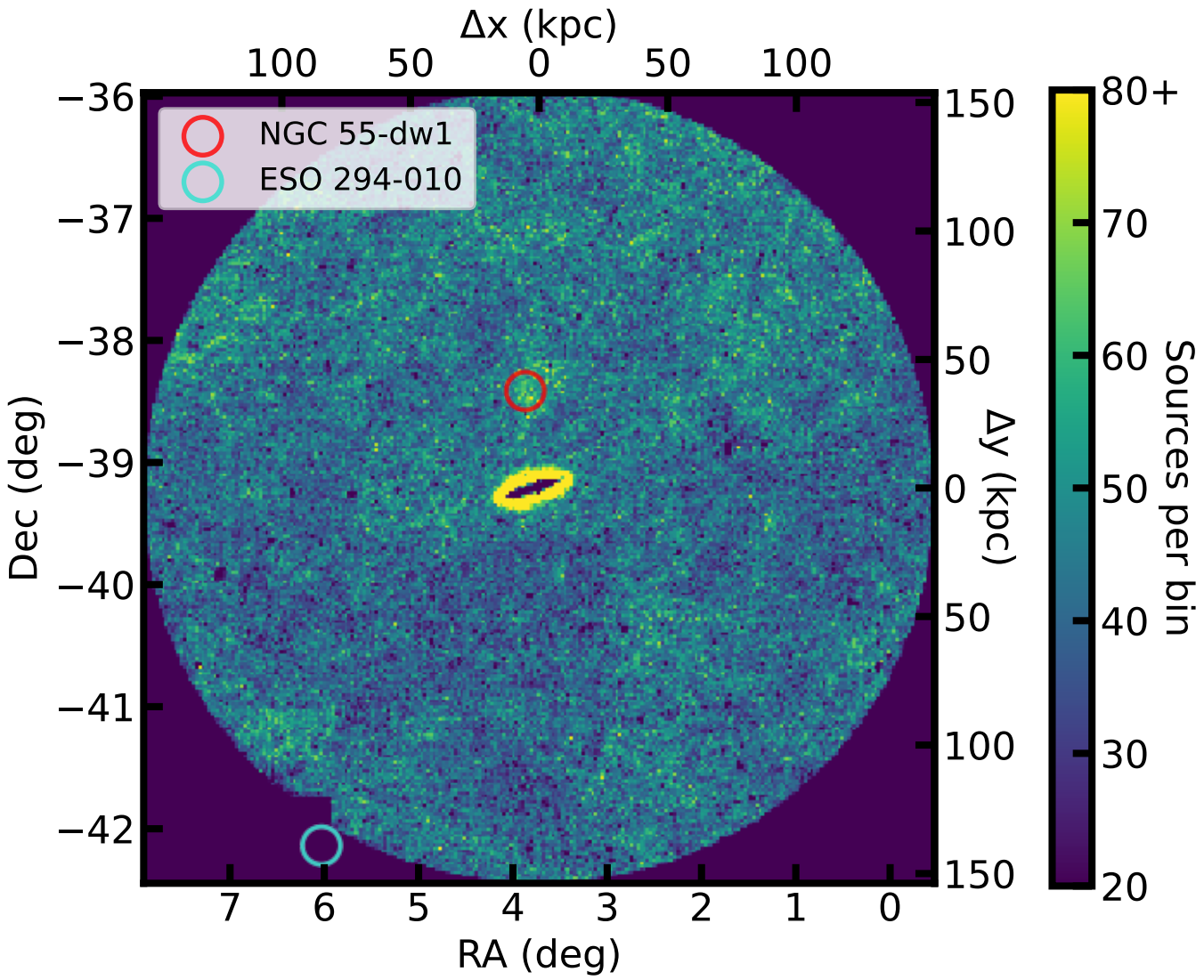


**Figure 3.** RGB density map of DELVE-DEEP's NGC 55 footprint (rad = 3.25 deg) with binsize = 1.5 arcmin$^2$. The color bar indicates the number of sources per bin. The two previously known NGC 55 satellites, NGC 55-dw1 and ESO 294-010, plotted in red and cyan, respectively. We note that, while ESO 294-010 is located slightly outside the DELVE-DEEP footprint, it lies just at the edge of the virial radius of NGC 55.

son, have relatively little effect on the number of sources detected. These criteria are as follows:

`(EXTENDED_CLASS_G != 0) & (EXTENDED_CLASS_I != 0)`,
`(SPREAD_MODEL_I + 5/3*SPREADERR_MODEL_I > 0.007)`,
`(MAG_AUTO_G - MAG_AUTO_I > -0.1)`,
`(MAG_AUTO_G - MAG_AUTO_I < 1.4)`.[2]

In addition to these LSB selection cuts, we also apply color and magnitude cuts similar to the RGB selection in Section 3.1, though these cuts have a negligible effect on the results of our dwarf search.

After applying these cuts, we bin the data into 1.5 arcmin$^2$ bins and apply the `find_peaks` function with the same `threshold` and `box_size` parameters as used in the analysis described in Section 3.1. This resulted in a list of 1,535 overdensities, which is significantly more than the 419 overdensities detected by the resolved method, since the LSB search picks up more false detections such as the halos of bright foreground stars and background galaxies. These detections are then filtered out through visual inspection.

It is important to note that, since star-galaxy separation is not applied, the resolved search includes all

[2] See Drlica-Wagner et al. (2022) Eq. 2 and Desai et al. (2012) for definitions of `EXTENDED_CLASS` and `SPREAD_MODEL`, respectively. `MAG_AUTO` is the automatic aperture magnitude calculated by `SourceExtractor`.

sources that are present in the semiresolved search. One might therefore expect that any overdensity detected in the semiresolved search would also appear in the resolved search. This is not the case, however, since the resolved search has a much higher average number of sources per bin, which reduces the relative significance of semiresolved overdensities, making them less likely to be detected.

### 3.3. *Visual Inspection*

Our dwarf search yields 419 candidates through the resolved detection method and 1,535 candidates through the semiresolved detection method, which, after removing duplicates, results in a total of 1,943 potential dwarf galaxy candidates. Visual inspection of these candidates was carried out using the citizen science platform, Zooniverse, with three members of our team classifying each candidate as either a potential dwarf galaxy worthy of further follow-up observation or as a false detection. For each candidate, we inspected a color-magnitude diagram, spatial distribution, radial density profile, LF, and color image (similar to the diagnostic plots described in Carlin et al. 2024). This visual inspection campaign resulted in zero 3-vote candidates, two 2-vote candidates, 268 1-vote candidates, and 1,720 0-vote candidates, where "X-vote" means that a candidate was classified by X number of people as a potential dwarf galaxy. Only those candidates receiving two or more votes were considered our most probable dwarf galaxy detections. Follow-up imaging for one of these two candidates was obtained using the Gemini Multi-Object Spectrograph (GMOS; Hook et al. 2004) on the Gemini South telescope, however these new data suggest that this candidate is not a real satellite of NGC 55. While no additional data were collected for the second candidate, its similarity to the first candidate suggests that it is likely either another background galaxy or galaxy cluster. See Appendix B for more information.

It should also be noted that while NGC 55-dw1 was detected by our resolved search method, it did not pass our visual inspection due to its extremely large size and LSB. We likely would have identified NGC 55-dw1 during visual inspection had we used a larger cutout size to generate candidate plots. However, to optimize the inspection process for the more typical sizes of dwarf galaxies expected in our search, we adopted a smaller field of view (3 arcmin$^2$), which is better suited to these dwarfs, though too small to capture the full extent of NGC 55-dw1.

## 4. ARTIFICIAL DWARF GALAXY SIMULATIONS

To properly interpret the results of our dwarf galaxy search, we need to characterize our detection depth and selection efficiency. To do this, we measure our dwarf galaxy detection sensitivity using artificial dwarf galaxy simulations. These simulations involve injecting artificial dwarfs into our data set and measuring the fraction of those that are recoverable. These injections are performed on the image level because dwarf galaxies at the distance of NGC 55 are not entirely resolved, and the unresolved portions of these galaxies can be more accurately modeled on the image level, as opposed to the catalog level (Garling et al. 2021). To obtain a representative sample of the whole NGC 55 footprint, we inject dwarfs into 26 of the 184 DELVE-DEEP NGC 55 coadded tiles (or "coadds") that vary in exposure time and limiting magnitude and span the full range of depths covered by the DELVE-DEEP fields in Figure 1.

To make sure our simulated galaxies are representative of real dwarfs, each simulated dwarf's stellar population is composed of old, metal-poor stars. Following Mutlu-Pakdil et al. (2021), each stellar population is sampled from an isochrone modeling a galaxy at distance $D_{NGC55}$ $\approx$ 2Mpc with an age of 10 Gyr and metallicity of [Fe/H] $= -2$, and generated according to a Salpeter IMF following $dN/dM \propto M^{-2.35}$ (Salpeter 1955). Isochrones are generated using the Dartmouth Stellar Evolution Database (Dotter et al. 2008). The stars within each dwarf's stellar population with $i \leq 27$ mag are modeled as point sources convolved with the observed PSF and injected individually into the images according to an exponential profile. Rather than repeating this process for the faint, unresolved stars below our detection limits, all the stars with $i > 27$ mag are instead modeled and injected as a single exponential galaxy profile, such that each artificial dwarf is comprised of both a resolved and unresolved component. Both the point sources and exponential profiles are modeled using the galaxy image simulation package, `galsim` (Rowe et al. 2015). Our tests demonstrate that our dwarf-search pipeline detects these artificial dwarfs just as effectively as those in which all stars are injected as individual point sources.

A total of 2,287 artificial dwarfs, uniformly sampled from half-light radii $1.8 \leq \log(r_h/\mathrm{pc}) \leq 3.2$ and absolute magnitudes $-6.0 \geq M_V \geq -9.0$, are created and injected into the set of 26 coadds. To convert from $g$- and $i$-band magnitudes to $M_V$, we use the SDSS color conversions in Jordi et al. (2006), which give nearly the same results as the DES color conversions in Abbott et al. (2021). Figure 4 shows four examples of artificial dwarf galaxies that are used in our analysis. We then treat the images with artificial dwarf galaxies in the same way as the unaltered images: each coadd is run through `SourceExtractor`, using the same parameters as in the DESDM processing of the real images.

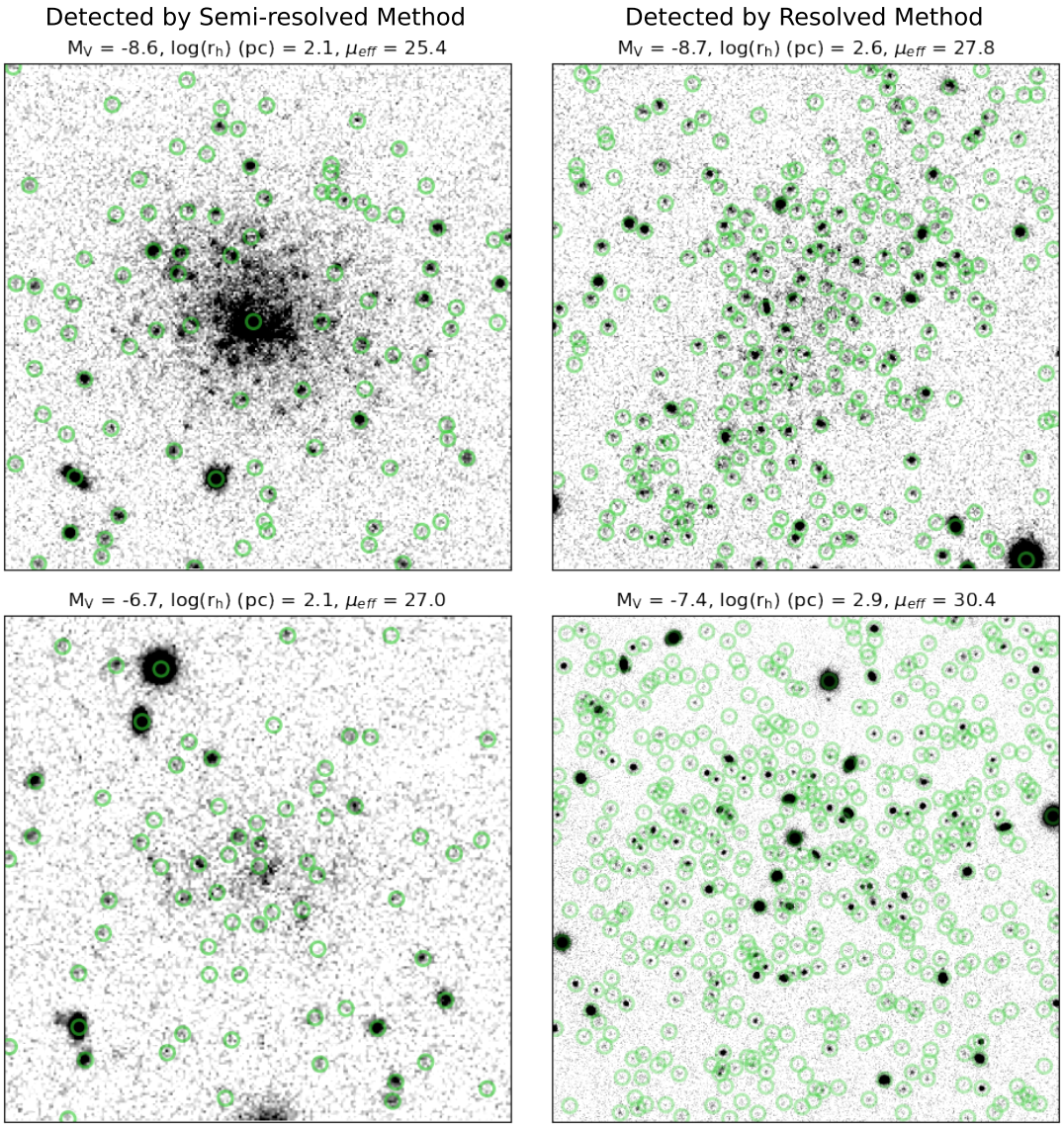


**Figure 4.** Four injected artificial dwarf galaxies of varying absolute magnitude, half-light radius, and effective surface brightness shown in $i$ band. Green circles indicate sources detected by `SourceExtractor`. Left column: Artificial dwarfs detected by our semiresolved method. Right column: Artificial dwarfs detected by our resolved method.

We run the resulting source catalogs through our dwarf-search pipeline (see Section 3) to investigate our detection rate as a function of dwarf size ($r_h$) and luminosity ($M_V$). First, however, we account for dwarfs that, due to randomness in our injection process, are injected into regions of the NGC 55 halo that are already overdense and, as a result, are detected by our pipeline regardless of their parameters. To address this, our dwarf-search pipeline is run on both the altered images with injected dwarfs as well as the unaltered images. Any bins detected as overdensities in the unaltered images are removed from the dwarf search on the altered images, so that any artificial dwarfs located in these bins are removed from our sample and do not contribute to our detection sensitivity calculation. After running our dwarf-search pipeline on each of the remaining artificial dwarfs, our team visually inspected each detection using Zooniverse. Just like in our real satellite search (see Section 3.3), each dwarf was visually inspected by three team members, and only those identified as dwarfs by at least two of the three are considered detections. Both this Zooniverse inspection and that of the real satellite search were performed simultaneously to avoid any biases that could have resulted from inspecting the real candidates and artificial dwarfs separately.

Our resulting detection sensitivity (see Figure 5) shows that the resolved detection method is more efficient for large, bright dwarf galaxies, while the semire-

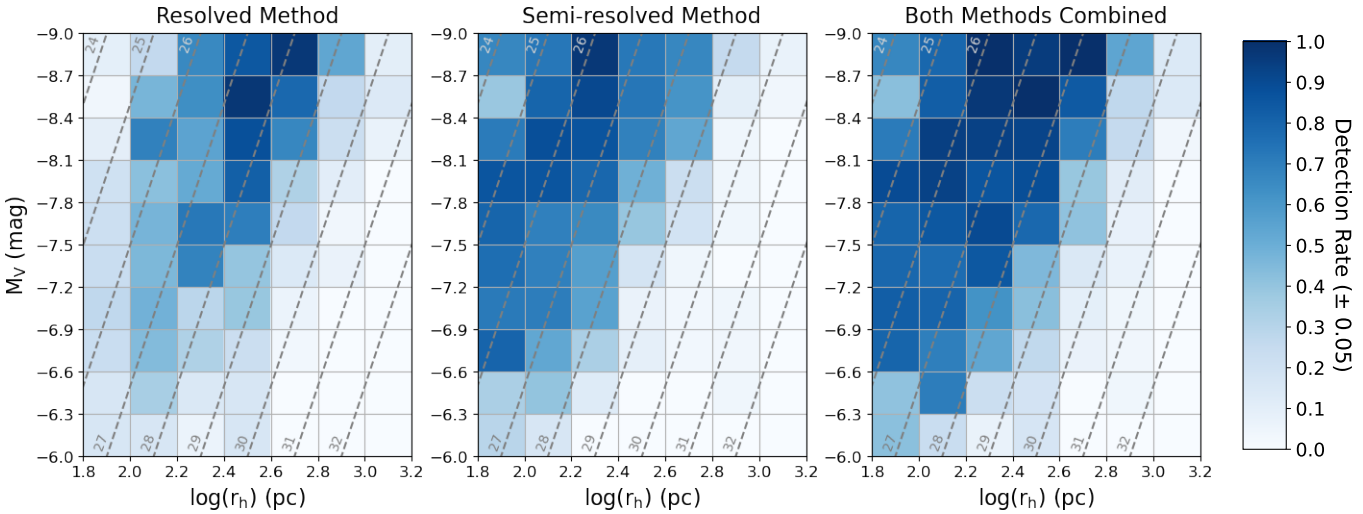


**Figure 5.** Dwarf galaxy detection sensitivity for each detection method individually (left and middle) and both methods combined (right). Detection rates have been corrected according to visual inspection results, where only artificial dwarfs that were classified as dwarfs by at least two people were counted as detections. Each bin contains, on average, 30 injected dwarfs with a standard deviation of 4. The corresponding average uncertainty in detection rate (calculated using binomial statistics) is 0.05. Lines of constant surface brightness are shown in gray (given in mag arcsec$^{-2}$). When convolved with the dwarf galaxy size-luminosity relation (Brasseur et al. 2011), we are $\sim 80\%$ complete for $M_V \lesssim -7.8$ and $\sim 50\%$ complete for $M_V \lesssim -7.0$.

solved method is more sensitive to faint, compact ones (i.e., those with less resolved stars due to blending effects). With these two methods combined (through an outer join[3]; see right panel), we are sensitive to both regimes and can detect dwarf galaxies with $\gtrsim 80\%$ efficiency, on average, with effective surface brightness $\mu_{\rm eff} \lesssim 28.5$ mag arcsec$^{-2}$ and $M_V \lesssim -6.6$. When these detection rates are convolved with the dwarf galaxy size-luminosity relation presented in Brasseur et al. (2011), we find that we are $\sim 80\%$ complete to dwarf galaxies with $M_V \lesssim -7.8$. Detection rates drop for faint, diffuse dwarf galaxies (bottom right of each panel), as well as for very bright and compact dwarfs (top left corner of each panel), because these systems can no longer be identified as overdensities of individual stars or unresolved light components. This highlights a known limitation in distinguishing between very compact, high surface brightness dwarfs and background galaxies in crowded fields. It is also worth noting that, while our detection rates drop significantly for dwarfs with $\mu_{\rm eff} \gtrsim 28.5$ mag arcsec$^{-2}$, many of these dwarfs (in particular, those with $M_V \lesssim -7.5$) were detected by our resolved search method, but were not identified during the visual inspection due to their diffuse nature (similar to NGC 55-dw1; see Section 3.3). Additionally, while our sensitivity likely extends to dwarfs with $\log(r_h/{\rm pc}) < 1.8$ ($r_h \lesssim 63$ pc), we chose not to explore this parameter space because there are currently very few known dwarf galaxies with $M_V \leq -6.0$ and $r_h \lesssim 63$ pc (Mutlu-Pakdil et al. 2021; Pace et al. 2022).

[3] Outer join means that the output tables of each detection method are combined such that all rows from both tables are included and duplicate rows are matched together. In `pandas.merge`, this corresponds to `how="outer"`.

## 5. DISCUSSION

We construct the satellite LF of NGC 55 that is roughly complete down to $M_V \sim -7$ and surface brightness $\mu_{\rm eff} \sim 28.5$ mag arcsec$^{-2}$ (see Figure 6). Our dwarf galaxy search (see Section 3) yielded no new satellites beyond the two previously known systems, ESO 294-010 and NGC 55-dw1. Only the former of these systems is included as part of our LF because NGC 55-dw1 is an extremely diffuse dwarf galaxy ($\mu_{\rm eff} \sim 32.3$ mag arcsec$^{-2}$; McNanna et al. 2024) and consequently falls below our completeness limits. It is because of this unusually diffuse nature that NGC 55-dw1 is not detected in our visual search (see Section 3.3). We include ESO 294-010 in our LF since its luminosity and surface brightness fall within the assumed extent of our completeness. Although ESO 294-010 is located near the edge of NGC 55's virial radius, just beyond our search radius, its similar distance and radial velocity to NGC 55 (see Table 1) suggest that it is a likely satellite. As a result, our LF consists of one NGC 55 satellite to which we are complete.

We compare our LF to two existing ΛCDM-based predictions of the satellite populations of LMC-mass hosts (see Carlin et al. 2024 for similar comparisons with the NGC 2403 satellite system). The blue-shaded region

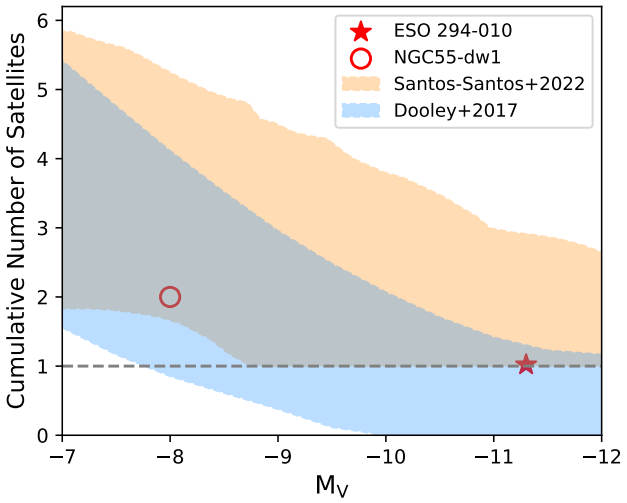


**Figure 6.** Satellite LF for NGC 55 down to $M_V = -7$ ($\sim 50\%$ completeness limit of our dwarf search) given by the gray-dashed line. ESO 294-010 is shown with a red star and NGC 55-dw1 is shown with a red circle. While NGC 55-dw1 is a confirmed satellite of NGC 55, it is not included as part of our LF due to it being outside the size range of our sensitivity. The orange- and blue-shaded regions correspond to predicted satellite populations for an LMC-mass host, adapted from the 80% scatter in Santos-Santos et al. (2022) and $1\sigma$ scatter in Dooley et al. (2017), respectively. Both of these regions have been convolved with our observed sensitivity.

in Figure 6 corresponds to the $1\sigma$ scatter in predicted satellites of an isolated, LMC-mass host, as presented in Dooley et al. (2017). These predictions are based on the *Caterpillar* dark matter halo simulations (Griffen et al. 2016) and stellar mass-halo mass relation of Garrison-Kimmel et al. (2016). The orange-shaded region represents the 10-90 percentile scatter in predicted satellites around each of the DELVE-DEEP MC analogs, from Santos-Santos et al. (2022) (specifically, this region corresponds to the "cut-off" model from Santos-Santos et al. 2022). It should be noted that this model starts counting the cumulative number of satellites at 1 rather than 0, thereby excluding the possibility that such hosts have no satellites. These predictions are based on the Local Group cosmological simulation, APOSTLE (Fattahi et al. 2016). In both the Dooley et al. (2017) and Santos-Santos et al. (2022) simulations, only subhalos within the virial radius of each primary halo were considered as potential satellites, making the corresponding predictions directly comparable to our LF for NGC 55, since our search was also restricted to the host's virial radius.

Both the blue and orange regions have been convolved with our observed sensitivity (Figure 5) and thus represent the predicted number of observed satellites rather than the number of satellites predicted by simulations. To perform these convolutions, it was necessary to determine our sensitivity as a function of only $M_V$, as opposed to both $M_V$ and $r_h$, which was achieved using the dwarf galaxy size-luminosity relation presented in Brasseur et al. (2011). With our sensitivity taken into account, our LF aligns well with both ΛCDM predictions. On the bright end it agrees closely with each of the predicted regions, while on the faint end it is slightly underpopulated.

Our LF is also in agreement with two recent LFs for the LMC analog, NGC 2403 (Carlin et al. 2024), and SMC analog, NGC 3109 (Doliva-Dolinsky et al. 2025), each of which contain two satellites with $-7 \geq M_V \geq -13$ around their respective hosts, and are consistent with ΛCDM predictions. Additionally, our LF is consistent with the results of two recent dwarf galaxy surveys targeting MC analogs at distances of $4 - 10$ Mpc: ID-MAGE (Hunter et al. 2025) and ELVES-Dwarf (Li et al. 2025). ID-MAGE reports an average of $4.0 \pm 1.4$ satellite candidates per LMC-mass host (with a lower bound of $1.4 \pm 0.6$ satellites), and ELVES-Dwarf finds $0 - 2$ satellites around each of their MC-mass hosts. Both of these bounds agree well with NGC 55 having two satellites. It is worth noting, however, that NGC 55 is significantly closer than the hosts targeted by ID-MAGE and ELVES-Dwarf. While these complementary surveys rely exclusively on integrated light detection—allowing them to probe a larger number of hosts—, they are limited in their ability to detect the faintest satellites. As a result, both surveys are complete only down to $M_V \sim -9$, roughly two magnitudes brighter than our completeness limit. The relative proximity of NGC 55 enables (semi)resolved star searches in our study, allowing us to reach significantly fainter systems that would otherwise remain undetectable.

In Figure 7, we place the two dwarf satellites of NGC 55 in context with other MC analogs in the size-luminosity plane. NGC 55's brighter satellite companion, ESO 294-010, is consistent with other known dwarfs in terms of size and luminosity ($M_V \sim -11.3$; $r_h \sim 248$ pc). In addition to an old, metal-poor stellar population, ESO 294-010 contains a small population of young, main-sequence stars as well as H I gas (Karachentsev et al. 2002; Da Costa et al. 2010). NGC 55-dw1, on the other hand, is similar in magnitude to a number of other known dwarfs, but is unusually large for its luminosity ($M_V \sim -8.0$; $r_h \sim 2.2$ kpc), which is possibly a result of tidal interactions with NGC 55 (McNanna et al. 2024). Additionally, the lack of deeper imaging around this dwarf makes it difficult

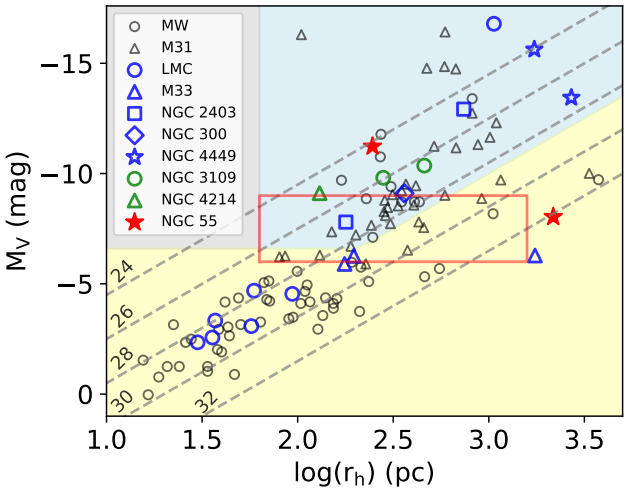


**Figure 7.** Absolute magnitude vs. half-light radius for known dwarf satellites. Open gray symbols indicate MW and M31 satellites from the compilation of Pace 2024. Open blue symbols indicate satellites of the LMC (Patel et al. 2020) or LMC analogs: M33 (Chapman et al. 2013; Martínez-Delgado et al. 2021; Collins et al. 2024; Ogami et al. 2024), NGC 2403 (Carlin et al. 2024), NGC 300 (Sand et al. 2024), NGC 4449 (Rich et al. 2012; Martínez-Delgado et al. 2012). Open green symbols indicate satellites of SMC analogs: NGC 3109 (Sharina et al. 2008; Sand et al. 2015; Doliva-Dolinsky et al. 2025), and NGC 4214 (Carlin et al. 2021). Closed red stars indicate NGC 55 satellites. The red rectangle outlines the parameter space that was tested in artificial dwarf simulations (Section 4). The light blue-shaded region indicates where our dwarf search is $\gtrsim 80\%$ complete, and the yellow-shaded region indicates where our search is $\lesssim 80\%$ complete. Completenesses in these regions outside of the red rectangle are extrapolated. The gray-shaded region indicates where we cannot extrapolate our completeness. Gray-dashed lines indicate lines of constant surface brightness.

to conclude whether or not it contains any young stellar populations. That said, NGC 55 appears to have a distorted H I disk with some gas extending in the direction of NGC 55-dw1, which could potentially be a sign of tidal interaction (Westmeier et al. 2013). Furthermore, the unusually diffuse nature of NGC 55-dw1 raises the question of whether it is truly an intact system or part of a larger tidal debris structure. While similarly diffuse dwarfs, such as Antlia II and Crater II, are generally regarded as gravitationally bound systems (Torrealba et al. 2016, 2019; Ji et al. 2021), the lack of dynamical observations for NGC 55-dw1 leaves its bound nature uncertain.

## 6. CONCLUSION

In this work, we perform a systematic satellite search around a nearby LMC-mass galaxy, NGC 55 (2.1 Mpc). Unlike previous satellite searches around low-mass hosts, our approach combines both resolved and semiresolved detection methods. As a result, our satellite search yields two potential dwarf galaxy candidates, although follow-up GMOS imaging for one of these candidates indicates that it is not a satellite of NGC 55, and the second candidate's similarity to the first suggests that it is not a satellite either (see Appendix B). We present a satellite LF for NGC 55 complete down to $M_V \sim -7$ that consists of one dwarf galaxy, ESO 294-010, with $M_V \sim -11.3$ (see Figure 6). We do not include NGC 55's second known satellite, NGC 55-dw1, in our LF because its unusually diffuse nature places it outside our completeness limits. Nevertheless, our LF is in good agreement with the ΛCDM predictions presented in Dooley et al. (2017) and Santos-Santos et al. (2022) and with the results of recent dwarf galaxy searches around other MC analogs (Carlin et al. 2024, Hunter et al. 2025, Doliva-Dolinsky et al. 2025, Li et al. 2025). Furthermore, when placed in context with other satellites of such MC analogs, ESO 294-010 demonstrates a size and luminosity consistent with those of similar systems, while NGC 55-dw1 is notably larger in comparison to other dwarfs with similar luminosities. This unusually extended structure could suggest that NGC 55-dw1 has undergone tidal disruption by NGC 55 or that it is not a completely intact satellite.

In determining the completeness of our satellite search, our artificial dwarf galaxy simulations show that the combination of resolved and semiresolved search methods results in the detection of a broad range of dwarf galaxy properties, since we are sensitive to dwarfs with $\mu_{\rm eff} \lesssim 28.5$ mag arcsec$^{-2}$ and $M_V \lesssim -6.6$ and $\sim 80\%$ complete to $M_V \lesssim -7.8$ (see Figure 5). This approach could therefore enhance the completeness and robustness of future satellite searches targeting a similar regime of dwarf galaxies. Machine learning techniques could be particularly adept at integrating both resolved and unresolved information to enhance the efficiency of such searches (e.g., Müller & Schnider 2021, Tanoglidis et al. 2021, Jones et al. 2023).

As one of the only comprehensive satellite studies around a low-mass host, our results emphasize the need to rigorously characterize additional MC-analog satellite systems. With recent and upcoming papers (Carlin et al. 2024; Doliva-Dolinsky et al. 2025) beginning to increase our sample of explored MC-mass hosts, the DELVE-DEEP survey will conduct satellite searches around its three remaining targets, further improving the characterization of satellites around low-mass hosts in the Local Volume. DELVE-DEEP will also perform systemic searches for substructures around the remaining hosts, as has recently been done for NGC 300

(Fielder et al. 2025). To complement this, the MADCASH survey will execute satellite and substructure searches around its five remaining MC-mass targets (Carlin et al. 2024). Within the next year, the Vera C. Rubin Observatory's Legacy Survey of Space and Time (LSST; Ivezić et al. 2019) will begin operations. LSST will likely be able to identify hundreds of new dwarf galaxies in the Southern sky, including both satellites of larger galaxies and isolated field dwarfs, allowing for a better evaluation of the ΛCDM model on small scales (Mutlu-Pakdil et al. 2021). Dwarf searches performed in the LSST era could also benefit from combining resolved and semiresolved search methods, as demonstrated in this work. This approach may enable the detection of more, and even fainter, dwarf galaxies than current predictions suggest.

## 7. ACKNOWLEDGEMENTS

We thank the anonymous reviewer for their careful reading of our manuscript and their insightful comments and suggestions. J.M. acknowledges support from the University of Chicago Quad Undergraduate Research Scholars Program. W.C. gratefully acknowledges support from a Gruber Science Fellowship at Yale University. This material is based upon work supported by the National Science Foundation Graduate Research Fellowship Program under Grant No. DGE2139841. Any opinions, findings, and conclusions or recommendations expressed in this material are those of the author(s) and do not necessarily reflect the views of the National Science Foundation.

This material is based upon work supported by the National Science Foundation under Grant No. AST-2108168, AST-2108169, AST-2307126, and AST-2407526. This research award is partially funded by a generous gift of Charles Simonyi to the NSF Division of Astronomical Sciences. The award is made in recognition of significant contributions to Rubin Observatory's Legacy Survey of Space and Time.

The DELVE Survey gratefully acknowledges support from Fermilab LDRD (L2019.011), the NASA Fermi Guest Investigator Program Cycle 9 (No. 91201), and the National Science Foundation (AST-2108168, AST-2307126). This work was supported in part by the U.S. Department of Energy, Office of Science, Office of Workforce Development for Teachers and Scientists (WDTS) under the Science Undergraduate Laboratory Internships Program (SULI).

This publication uses data generated via the Zooniverse.org platform, development of which is funded by generous support, including a Global Impact Award from Google, and by a grant from the Alfred P. Sloan Foundation.

This project used data obtained with the Dark Energy Camera (DECam), which was constructed by the Dark Energy Survey (DES) collaboration. Funding for the DES Projects has been provided by the DOE and NSF (USA), MISE (Spain), STFC (UK), HEFCE (UK), NCSA (UIUC), KICP (U. Chicago), CCAPP (Ohio State), MIFPA (Texas A&M), CNPQ, FAPERJ, FINEP (Brazil), MINECO (Spain), DFG (Germany) and the Collaborating Institutions in the Dark Energy Survey, which are Argonne Lab, UC Santa Cruz, University of Cambridge, CIEMAT-Madrid, University of Chicago, University College London, DES-Brazil Consortium, University of Edinburgh, ETH Zürich, Fermilab, University of Illinois, ICE (IEEC-CSIC), IFAE Barcelona, Lawrence Berkeley Lab, LMU München and the associated Excellence Cluster Universe, University of Michigan, NOIRLab, University of Nottingham, Ohio State University, OzDES Membership Consortium, University of Pennsylvania, University of Portsmouth, SLAC National Lab, Stanford University, University of Sussex, and Texas A&M University.

Based on observations at Cerro Tololo Inter-American Observatory at NSF's NOIRLab (NOIRLab Prop. ID 2019A-0305; PI: A. Drlica-Wagner), which is managed by the Association of Universities for Research in Astronomy (AURA) under a cooperative agreement with the National Science Foundation.

Based on observations obtained at the international Gemini Observatory (GS-2024B-FT-204; PI: J. Medoff), a program of NSF NOIRLab, which is managed by the Association of Universities for Research in Astronomy (AURA) under a cooperative agreement with the U.S. National Science Foundation on behalf of the Gemini Observatory partnership: the U.S. National Science Foundation (United States), National Research Council (Canada), Agencia Nacional de Investigación y Desarrollo (Chile), Ministerio de Ciencia, Tecnología e Innovación (Argentina), Ministério da Ciência, Tecnologia, Inovações e Comunicações (Brazil), and Korea Astronomy and Space Science Institute (Republic of Korea).

*Facilities:* Blanco

*Software:* Astropy (Astropy Collaboration et al. 2013, 2018)

## REFERENCES

Abbott, T. M. C., Adamów, M., Aguena, M., et al. 2021, ApJS, 255, 20
Arias, J. M., Bell, E. F., Gozman, K., et al. 2025, The Astrophysical Journal Letters, 982, L3. https://dx.doi.org/10.3847/2041-8213/adb433
Astropy Collaboration, Robitaille, T. P., Tollerud, E. J., et al. 2013, A&A, 558, A33
Astropy Collaboration, Price-Whelan, A. M., Sipőcz, B. M., et al. 2018, AJ, 156, 123
Bechtol, K., Drlica-Wagner, A., Balbinot, E., et al. 2015, ApJ, 807, 50
Belokurov, V., Zucker, D. B., Evans, N. W., et al. 2006, The Astrophysical Journal, 647, L111. https://dx.doi.org/10.1086/507324
Bennet, P., Sand, D. J., Crnojević, D., et al. 2019, ApJ, 885, 153
—. 2020, ApJL, 893, L9
Bertin, E. 2010, SCAMP: Automatic Astrometric and Photometric Calibration, Astrophysics Source Code Library, record ascl:1010.063, ,
Bertin, E., & Arnouts, S. 1996, A&AS, 117, 393
Brasseur, C. M., Martin, N. F., Macciò, A. V., Rix, H.-W., & Kang, X. 2011, The Astrophysical Journal, 743, 179
Bullock, J. S., & Boylan-Kolchin, M. 2017, ARA&A, 55, 343
Carlin, J. L., Sand, D. J., Price, P., et al. 2016, ApJL, 828, L5
Carlin, J. L., Mutlu-Pakdil, B., Crnojević, D., et al. 2021, ApJ, 909, 211
Carlin, J. L., Sand, D. J., Mutlu-Pakdil, B., et al. 2024, arXiv e-prints, arXiv:2409.17437
Carlsten, S. G., Greene, J. E., Beaton, R. L., Danieli, S., & Greco, J. P. 2022, ApJ, 933, 47
Cerny, W., Pace, A. B., Drlica-Wagner, A., et al. 2021a, ApJ, 910, 18
—. 2021b, ApJL, 920, L44
Cerny, W., Martínez-Vázquez, C. E., Drlica-Wagner, A., et al. 2023, ApJ, 953, 1
Chapman, S. C., Widrow, L., Collins, M. L. M., et al. 2013, MNRAS, 430, 37
Chiboucas, K., Karachentsev, I. D., & Tully, R. B. 2009, AJ, 137, 3009
Collins, M. L. M., Karim, N., Martinez-Delgado, D., et al. 2024, Pisces VII/Triangulum III – M33's second dwarf satellite galaxy, , , arXiv:2305.13966. https://arxiv.org/abs/2305.13966
Crnojević, D., Sand, D. J., Spekkens, K., et al. 2016, ApJ, 823, 19
Crnojević, D., Sand, D. J., Bennet, P., et al. 2019, ApJ, 872, 80
Da Costa, G. S., Rejkuba, M., Jerjen, H., & Grebel, E. K. 2010, ApJL, 708, L121
Dalcanton, J. J., Williams, B. F., Seth, A. C., et al. 2009, ApJS, 183, 67
Davis, A. B., Nierenberg, A. M., Peter, A. H. G., et al. 2021, MNRAS, 500, 3854
de Vaucouleurs, G., de Vaucouleurs, A., Corwin, Herold G., J., et al. 1991, Third Reference Catalogue of Bright Galaxies
DES Collaboration, Abbott, T. M. C., Abdalla, F. B., et al. 2018, PhRvD, 98, 043526
Desai, S., Armstrong, R., Mohr, J. J., et al. 2012, ApJ, 757, 83
Doliva-Dolinsky, A., Martin, N. F., Thomas, G. F., et al. 2022, The Astrophysical Journal, 933, 135. https://dx.doi.org/10.3847/1538-4357/ac6fd5
Doliva-Dolinsky, A., Martin, N. F., Yuan, Z., et al. 2023, The Astrophysical Journal, 952, 72. https://dx.doi.org/10.3847/1538-4357/acdcf6
Doliva-Dolinsky, A., Mutlu-Pakdil, B., Crnojević, D., et al. 2025, The Astrophysical Journal, 989, 21. https://dx.doi.org/10.3847/1538-4357/ade9b8
Dooley, G. A., Peter, A. H. G., Carlin, J. L., et al. 2017, MNRAS, 472, 1060
Dotter, A., Chaboyer, B., Jevremović, D., et al. 2008, ApJS, 178, 89
Drlica-Wagner, A., Bechtol, K., Rykoff, E. S., et al. 2015, ApJ, 813, 109
Drlica-Wagner, A., Carlin, J. L., Nidever, D. L., et al. 2021, ApJS, 256, 2
Drlica-Wagner, A., Ferguson, P. S., Adamów, M., et al. 2022, ApJS, 261, 38
Fattahi, A., Navarro, J. F., Sawala, T., et al. 2016, Monthly Notices of the Royal Astronomical Society, 457, 844. https://doi.org/10.1093/mnras/stv2970
Fielder, C. E., Sand, D. J., Jones, M. G., et al. 2025, Streams, Shells, and Substructures in the Accretion-Built Stellar Halo of NGC 300, , , arXiv:2501.04089. https://arxiv.org/abs/2501.04089
Flaugher, B., Diehl, H. T., Honscheid, K., et al. 2015, AJ, 150, 150
Garling, C. T., Peter, A. H. G., Kochanek, C. S., Sand, D. J., & Crnojević, D. 2021, arXiv e-prints, arXiv:2105.01082
Garrison-Kimmel, S., Bullock, J. S., Boylan-Kolchin, M., & Bardwell, E. 2016, Monthly Notices of the Royal Astronomical Society, 464, 3108. https://doi.org/10.1093/mnras/stw2564
Gil de Paz, A., Boissier, S., Madore, B. F., et al. 2007, ApJS, 173, 185

Griffen, B. F., Ji, A. P., Dooley, G. A., et al. 2016, The Astrophysical Journal, 818, 10. https://dx.doi.org/10.3847/0004-637X/818/1/10
Homma, D., Chiba, M., Komiyama, Y., et al. 2024, PASJ, 76, 733
Hook, I. M., Jørgensen, I., Allington-Smith, J. R., et al. 2004, PASP, 116, 425
Hunter, L. C., Mutlu-Pakdİl, B., Sand, D. J., et al. 2025, The Astrophysical Journal, 989, 58. https://dx.doi.org/10.3847/1538-4357/ade9a4
Ivezić, Ž., Kahn, S. M., Tyson, J. A., et al. 2019, ApJ, 873, 111
Jerjen, H., Freeman, K. C., & Binggeli, B. 1998, AJ, 116, 2873
Jethwa, P., Erkal, D., & Belokurov, V. 2016, Monthly Notices of the Royal Astronomical Society, 461, 2212. https://doi.org/10.1093/mnras/stw1343
Ji, A. P., Koposov, S. E., Li, T. S., et al. 2021, ApJ, 921, 32
Jones, M. G., Mutlu-Pakdil, B., Sand, D. J., et al. 2023, ApJL, 957, L5
Jordi, K., Grebel, E. K., & Ammon, K. 2006, A&A, 460, 339
Karachentsev, I. D., Makarov, D. I., & Kaisina, E. I. 2013, AJ, 145, 101
Karachentsev, I. D., Sharina, M. E., Makarov, D. I., et al. 2002, A&A, 389, 812
Karachentsev, I. D., Grebel, E. K., Sharina, M. E., et al. 2003, A&A, 404, 93
Koposov, S. E., Belokurov, V., Torrealba, G., & Evans, N. W. 2015, ApJ, 805, 130
Labrie, K., Simpson, C., Cardenes, R., et al. 2023, Research Notes of the American Astronomical Society, 7, 214
Li, J., Greene, J. E., Danieli, S., et al. 2025, arXiv e-prints, arXiv:2504.08030
Mao, Y.-Y., Geha, M., Wechsler, R. H., et al. 2024, arXiv e-prints, arXiv:2404.14498
Martin, N. F., Ibata, R. A., McConnachie, A. W., et al. 2013, ApJ, 776, 80
Martin, N. F., Ibata, R. A., Lewis, G. F., et al. 2016, ApJ, 833, 167
Martínez-Delgado, D., Karim, N., Charles, E. J. E., et al. 2021, Monthly Notices of the Royal Astronomical Society, 509, 16–24. http://dx.doi.org/10.1093/mnras/stab2797
Martínez-Delgado, D., Romanowsky, A. J., Jay Gabany, R., et al. 2012, The Astrophysical Journal, 748, L24. http://dx.doi.org/10.1088/2041-8205/748/2/L24
Mau, S., Cerny, W., Pace, A. B., et al. 2020, ApJ, 890, 136
McConnachie, A. W. 2012, AJ, 144, 4
McNanna, M., Bechtol, K., Mau, S., et al. 2024, ApJ, 961, 126
McQuinn, K. B. W., Mao, Y.-Y., Buckley, M. R., et al. 2023, ApJ, 944, 14
McQuinn, K. B. W., Mao, Y.-Y., Tollerud, E. J., et al. 2024, ApJ, 967, 161
Morganson, E., Gruendl, R. A., Menanteau, F., et al. 2018, PASP, 130, 074501
Moustakas, J., Lang, D., Dey, A., et al. 2023, ApJS, 269, 3
Müller, O., & Schnider, E. 2021, The Open Journal of Astrophysics, 4, 3
Mutlu-Pakdil, B., Sand, D. J., Carlin, J. L., et al. 2018, ApJ, 863, 25
Mutlu-Pakdil, B., Sand, D. J., Crnojević, D., et al. 2021, arXiv e-prints, arXiv:2105.01658
—. 2024, ApJ, 966, 188
Ogami, I., Komiyama, Y., Chiba, M., et al. 2024, Triangulum IV: A Possible Ultra-Diffuse Satellite of M33, , , arXiv:2407.07481. https://arxiv.org/abs/2407.07481
Pace, A. B. 2024, arXiv e-prints, arXiv:2411.07424
Pace, A. B., Erkal, D., & Li, T. S. 2022, ApJ, 940, 136
Patel, E., Kallivayalil, N., Garavito-Camargo, N., et al. 2020, The Astrophysical Journal, 893, 121. http://dx.doi.org/10.3847/1538-4357/ab7b75
Planck Collaboration, Aghanim, N., Akrami, Y., et al. 2020, A&A, 641, A6
Prole, D. J., Davies, J. I., Keenan, O. C., & Davies, L. J. M. 2018, MNRAS, 478, 667
Rich, R. M., Collins, M. L. M., Black, C. M., et al. 2012, Nature, 482, 192–194. http://dx.doi.org/10.1038/nature10837
Rowe, B., Jarvis, M., Mandelbaum, R., et al. 2015, GalSim: The modular galaxy image simulation toolkit, , , arXiv:1407.7676
Salpeter, E. E. 1955, ApJ, 121, 161
Sand, D. J., Spekkens, K., Crnojević, D., et al. 2015, ApJL, 812, L13
Sand, D. J., Mutlu-Pakdil, B., Jones, M. G., et al. 2024, Three Quenched, Faint Dwarf Galaxies in the Direction of NGC 300: New Probes of Reionization and Internal Feedback, , , arXiv:2409.16345. https://arxiv.org/abs/2409.16345
Santos-Santos, I. M. E., Sales, L. V., Fattahi, A., & Navarro, J. F. 2022, MNRAS, 515, 3685
Schlafly, E. F., & Finkbeiner, D. P. 2011, ApJ, 737, 103
Sharina, M. E., Karachentsev, I. D., Dolphin, A. E., et al. 2008, MNRAS, 384, 1544
Simon, J. D. 2019, ARA&A, 57, 375
Simon, J. D., & Geha, M. 2007, ApJ, 670, 313
Smercina, A., Bell, E. F., Price, P. A., et al. 2018, ApJ, 863, 152

Smith, S. E. T., McConnachie, A. W., Gwyn, S., et al. 2025, arXiv e-prints, arXiv:2502.09792

Stetson, P. B. 1987, PASP, 99, 191

—. 1994, PASP, 106, 250

Tan, C. Y., Cerny, W., Drlica-Wagner, A., et al. 2024, arXiv:2408.00865. https://arxiv.org/abs/2408.00865

Tanoglidis, D., Drlica-Wagner, A., Wei, K., et al. 2021, ApJS, 252, 18

Torrealba, G., Koposov, S. E., Belokurov, V., & Irwin, M. 2016, MNRAS, 459, 2370

Torrealba, G., Belokurov, V., Koposov, S. E., et al. 2019, MNRAS, 488, 2743

Westmeier, T., Koribalski, B. S., & Braun, R. 2013, MNRAS, 434, 3511

Willman, B., Dalcanton, J. J., Martinez-Delgado, D., et al. 2005, The Astrophysical Journal, 626, L85. https://dx.doi.org/10.1086/431760

# APPENDIX

## A. STELLAR COMPLETENESS

To measure our stellar completeness, we inject artificial stars into our data set and measure the fraction of those that are recoverable. Like in Section 4, stars are injected on the image level and into the same set of 26 NGC 55 coadds.

Artificial stars are modeled as point sources convolved with the observed PSF using the galaxy image simulation package, `galsim` (Rowe et al. 2015). Square grids of 5,000-10,000 stars are injected into each of the 26 coadds with random g-band magnitudes between $21 \leq g \leq 27$ mag. To avoid significantly increasing the average background magnitude, the exact number of stars injected into each coadd was ∼10% of the number of real sources in the coadd. The colors of the artificial stars (and as a result, their $r$ and $i$ magnitudes) in each coadd are randomly sampled from the color distribution of real sources in that coadd ($-0.50 \lesssim g - r \lesssim 1.25$ and $-0.50 \lesssim g - i \lesssim 2.00$). This process is repeated for each coadd 10 times, resulting in a total of 260 coadds containing injected stars. Each coadd is then run through `SourceExtractor` for recovery, using the same parameters as in the DESDM processing of the real images.

After running this pipeline on the coadds containing artificial sources, the completeness of each coadd is determined by calculating the fraction of injected stars that are recovered as a function of input magnitude. Since we are not applying star-galaxy separation, stars are considered recovered as long as they are detected by `SourceExtractor` regardless of whether they are classified as point sources. Our measured completenesses are then fitted according to the completeness model described in Eq. 7 of Martin et al. 2016, which takes the form of a decreasing logistic function. The average completenesses across the 26 tested coadds are shown in Figure 8.

Our tests show that we are, on average, 90% complete to $g = 25.3 \pm 0.2$ mag and $i = 24.6 \pm 0.2$ mag, which are $\sim 1.0$ and $\sim 2.0$ mag fainter than the corresponding TRGB magnitudes, $m_g^{\rm TRGB} \sim 24.3$ and $m_i^{\rm TRGB} \sim 22.6$ (see Figure 8). These TRGB magnitudes are estimated using an old, metal-poor isochrone with [Fe/H] $= -2$ and age $= 10$ Gyr at the distance of NGC 55. Isochrones are generated using the Dartmouth Stellar Evolution Database (Dotter et al. 2008).

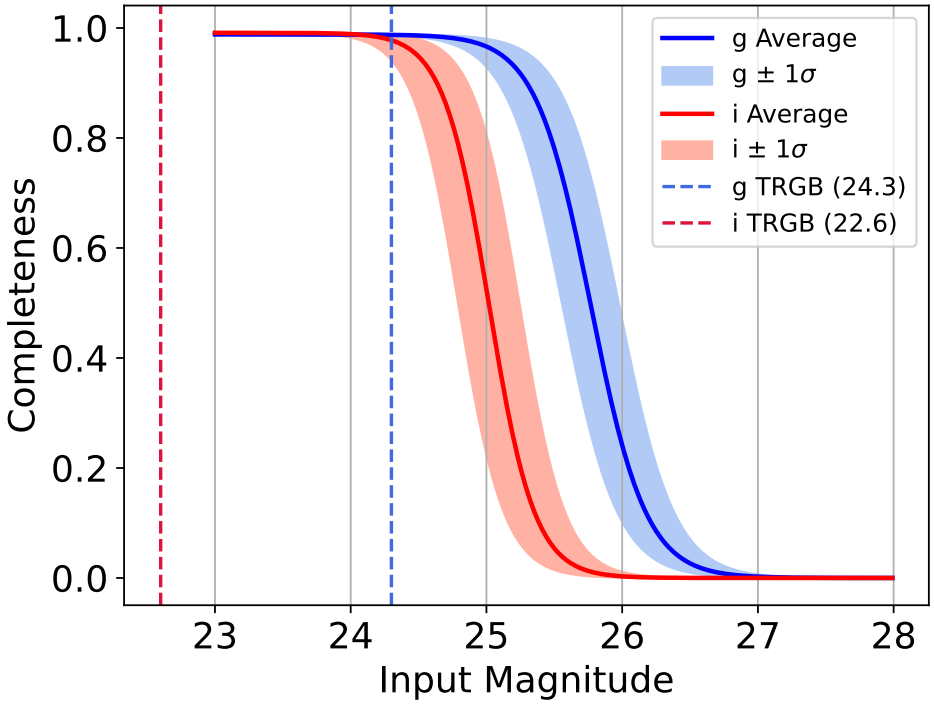


**Figure 8.** Average completeness in $g$ and $i$ bands across all 26 coadds used for the artificial star injections. Solid lines indicate mean completeness and shaded regions indicate $\pm 1\sigma$. Average 50% completeness is $25.8 \pm 0.2$ mag in $g$ and $25.0 \pm 0.2$ mag in $i$. TRGB apparent magnitudes in $g$ and $i$ given by blue- and red-dashed lines, respectively ($m_g^{\rm TRGB} \sim 24.3$; $m_i^{\rm TRGB} \sim 22.6$).

## B. TWO SATELLITE CANDIDATES

Figure 9 shows DELVE-DEEP images and color-magnitude diagrams of each of the 2-vote candidates that resulted from our satellite search. Note that the first of these candidates is detected by our resolved search method, whereas the second is detected by our semiresolved search method, despite both exhibiting overdensities of resolved stars, which is why we include a color-magnitude diagram for each. Brown points indicate sources that are not classified as stars, blue points represent sources identified as stars through star-galaxy separation, and red points highlight stars within our RGB selection region. Only the sources within a 0.3 arcmin radius from the candidate's center, marked by a red circle in the middle panel, are shown in the left panel. These sources are highlighted with corresponding colors on the $i$-band image in the right panel.

We obtained the follow-up imaging for the first of these two candidates with the Gemini Multi-Object Spectrograph (GMOS; Hook et al. 2004) on the Gemini South telescope (GS-2024B-FT-204; PI: J. Medoff). The GMOS images have a $\sim$5.5′×5.5′field of view and 0.16″pixel$^{-1}$ scale after binning. Both $g$ and $i$-band imaging was taken with strict image quality constraints on 2024 December 25 (UT). We collected 9×300 s $g$-band exposures and 4×300 s $i$-band exposures, with small dithers between each exposure. The goal of these follow-up observations was to increase the number of putative member stars in our candidate system in order to confirm whether they represented bona fide associations of stars at the distance of NGC 55.

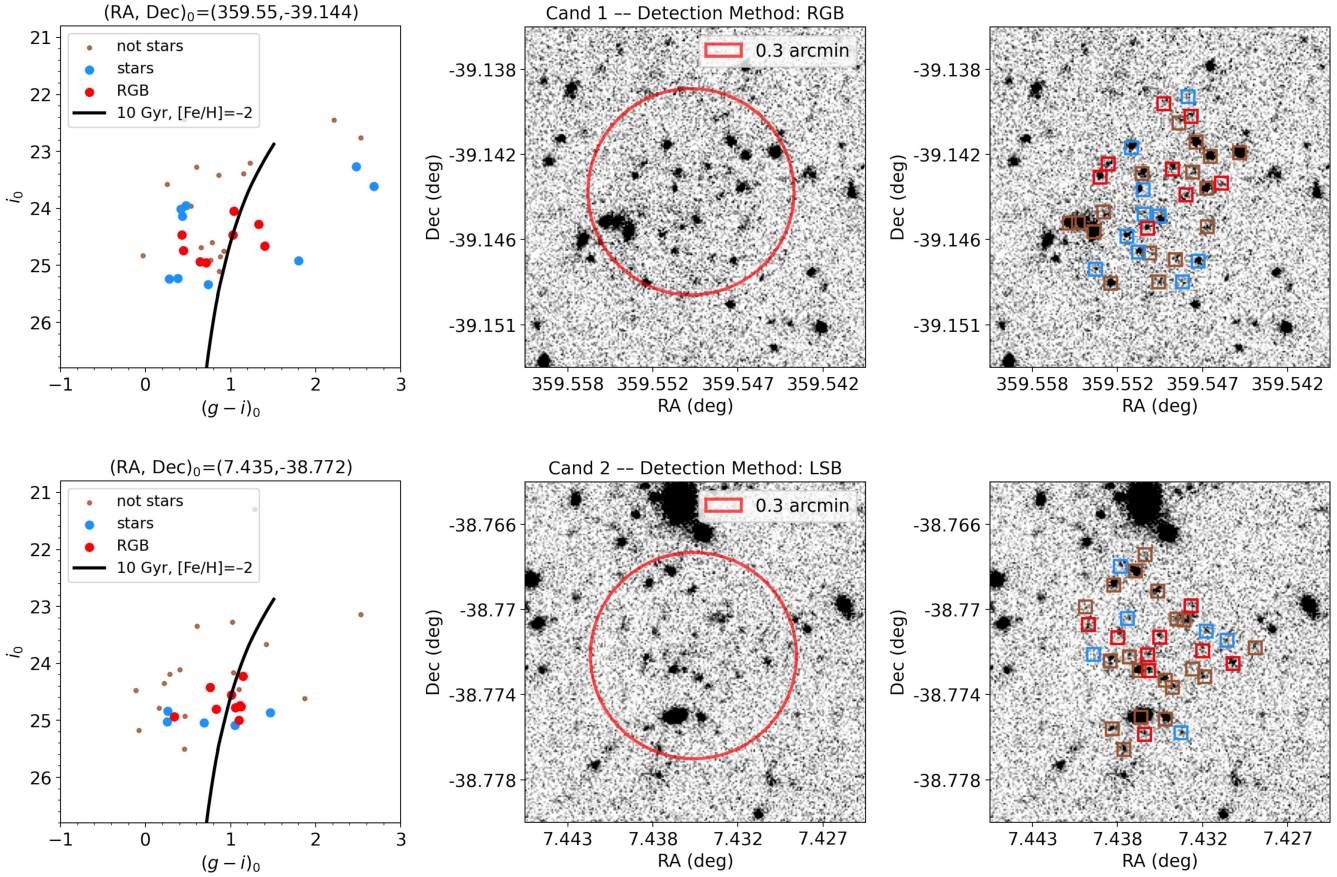


**Figure 9.** The DELVE-DEEP color-magnitude diagram of our 2-vote candidates (top: Candidate 1, bottom: Candidate 2) and their $i$-band images. RGB stars are shown in red, stars outside of our RGB selection region are shown in blue, and all other sources are shown in brown. The black line represents an old, metal-poor isochrone (age = 10 Gyr, [Fe/H]= −2, Dotter et al. 2008) at the distance of NGC 55. The left panel includes only the sources within a radius of 0.3 arcmin surrounding the candidate, indicated by the red circle in the middle panel. The corresponding detection method is given in the title. The right panel highlights each source from the left panel on the $i$-band image.

Initial data reduction was conducted using DRAGONS (Labrie et al. 2023), the pipeline maintained by Gemini Observatory. DRAGONS performs bias subtraction, flat-field correction, and bad pixel masking on the images. Cosmic rays were removed using the sigma-clipping method within the DRAGONS pipeline. Stacked images were created using the weighted average of the individual exposures. An astrometric correction was applied by using SCAMP (Bertin 2010). The final $g$- and $i$-band stacked images had PSF FWHM values around $0.7''$.

We performed PSF fitting photometry on the stacked GMOS images, using DAOPHOT and ALLFRAME (Stetson 1987, 1994), following the general procedure described in Mutlu-Pakdil et al. (2018). The photometry was calibrated to point sources in our DELVE-DEEP catalog, including a color term, and was corrected for Galactic extinction (Schlafly & Finkbeiner 2011) on a star-by-star basis. In Figure 10, we show the deep CMD of candidate 1 within a radius of $0.3'$, along with a representative background field of the same area. The overplotted red line represents an old, metal-poor isochrone (age = 10 Gyr; [Fe/H] = −2; Dotter et al. 2008) at the distance of NGC 55. The absence of stars near the isochrone and the overwhelming presence of background sources suggest that the candidate is not a real system at the distance of NGC 55.

No follow-up data were obtained for the second candidate (see Figure 9-bottom panels), but its similarity in appearance and the CMD to the first candidate suggests that it is unlikely to be a real system at the distance of NGC 55. In addition, both candidates are visible in the Wide-field Infrared Survey Explorer (WISE) data, specifically the unWISE W1/W2 NEO7 images. This may indicate that they are, instead, background, high-redshift galaxy clusters.

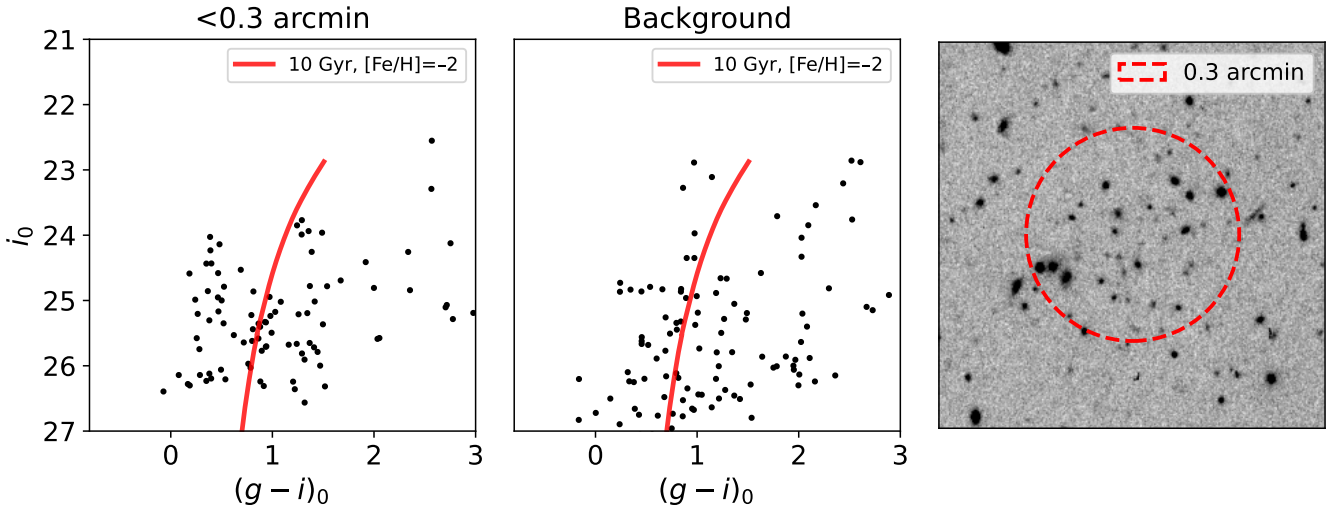


**Figure 10.** Follow-up Gemini data for Candidate 1. Left: Deep color-magnitude diagram of the region within a 0.3 arcmin radius of the candidate. Isochrone with age = 10 Gyr and metallicity [Fe/H] = −2 at the distance of NGC 55 is shown in red (Dotter et al. 2008). Middle: Same as left but for a background region of equal area. Right: An $i$-band image with a dashed red circle of a radius 0.3 arcmin surrounding the candidate.